Hyperuniform Monocrystalline Structures by Spinodal Solid-State Dewetting

Marco Salvalaglio,[1,2,*] Mohammed Bouabdellaoui,[3] Monica Bollani,[4,†] Abdennacer Benali,[3] Luc Favre,[3] Jean-Benoit Claude,[5] Jerome Wenger,[5] Pietro de Anna,[6] Francesca Intonti,[7] Axel Voigt,[1,2] and Marco Abbarchi[3,‡]

[1]*Institute of Scientific Computing, TU Dresden, 01062 Dresden, Germany*
[2]*Dresden Center for Computational Materials Science (DCMS), TU Dresden, 01062 Dresden, Germany*
[3]*Aix Marseille Univ, Université de Toulon, CNRS, IM2NP 13397, Marseille, France*
[4]*Istituto di Fotonica e Nanotecnologie-Consiglio Nazionale delle Ricerche, Laboratory for Nanostructure Epitaxy and Spintronics on Silicon, Via Anzani 42, 22100 Como, Italy*
[5]*Aix Marseille Université, CNRS, Centrale Marseille, Institut Fresnel, 13013 Marseille, France*
[6]*Institut des Sciences de la Terre, University of Lausanne, Lausanne 1015, Switzerland*
[7]*LENS, University of Florence, Sesto Fiorentino 50019, Italy*

(Received 3 March 2020; accepted 7 August 2020; published 15 September 2020)

Materials featuring anomalous suppression of density fluctuations over large length scales are emerging systems known as disordered hyperuniform. The underlying hidden order renders them appealing for several applications, such as light management and topologically protected electronic states. These applications require scalable fabrication, which is hard to achieve with available top-down approaches. Theoretically, it is known that spinodal decomposition can lead to disordered hyperuniform architectures. Spontaneous formation of stable patterns could thus be a viable path for the bottom-up fabrication of these materials. Here, we show that monocrystalline semiconductor-based structures, in particular $Si_{1-x}Ge_x$ layers deposited on silicon-on-insulator substrates, can undergo spinodal solid-state dewetting featuring correlated disorder with an effective hyperuniform character. Nano- to micrometric sized structures targeting specific morphologies and hyperuniform character can be obtained, proving the generality of the approach and paving the way for technological applications of disordered hyperuniform metamaterials. Phase-field simulations explain the underlying nonlinear dynamics and the physical origin of the emerging patterns.

DOI: 10.1103/PhysRevLett.125.126101

Disordered hyperuniform materials are an emerging class of systems featuring anomalous suppression of density fluctuations on large length scales [1–4]. While not presenting any Bragg peak in diffraction (as a liquid), they have strongly suppressed density fluctuations at long distances (as an ordered crystal). The underlying hidden order results in exotic phenomena, such as topologically protected electronic states [5], glassy electronic quantum state transitions [6], Anderson localization of light [7], polarization selectivity [8], lasing [9], and a full photonic band gap for light propagation [10–13].

Patterns exhibiting correlated disorder are ubiquitous in nature and are typical of many phenomena ruled by far-from-equilibrium processes [14,15]. Prominent examples are morphogenesis in biological systems [16], thin-layer wrinkling [17,18], and phase separation [19]. In these systems the presence of interactions and the underlying nonlinear dynamics lead to the formation of complex patterns eventually featuring correlated disorder [20]. Such patterns can emerge from phenomena involving long-range interactions and have been reported in thin films of polymers [21,22] and liquid metals [20]. Moreover, phase separation by spinodal decomposition has been recently proposed as a possible bottom-up process for producing hyperuniform materials [23,24].

Liquid thin films of metals and polymers can break and dewet through the amplification of uniformly distributed surface undulations [20–22]. Owing to the similarities of the final morphologies to those observed in phase separation via spinodal decomposition, this process is commonly termed spinodal dewetting. *De facto*, this regime has remained mostly inaccessible in the technologically relevant case of semiconductors and, more generally, in monocrystalline systems. Indeed, in thin crystalline films [21,25] the melting temperature is typically too high, rendering impossible to access the same spinodal dewetting dynamics. Instead, they undergo heterogeneous nucleation of holes, rim formation, and retraction, followed by finger and island formation well below their melting temperature. Owing to the anisotropic surface diffusion, the islands are aligned along the crystallographic directions and are formed at a typical distance set by the initial layer thickness [26].

Here, we report on the annealing of semiconductor, monocrystalline, thin films showing that (1) they can

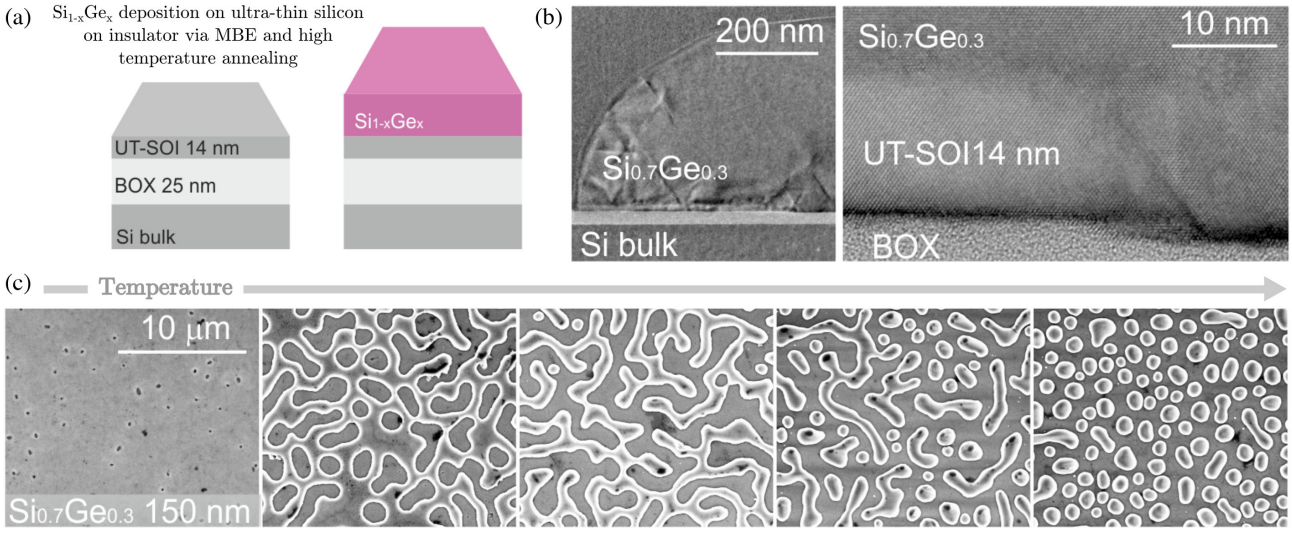

FIG. 1. Spinodal solid-state dewetting. (a) Scheme of the samples: ultrathin silicon on insulator substrates (14 nm thick Si on 25 nm thick SiO_2 BOX) followed by epitaxial deposition of $Si_{1-x}Ge_x$ alloys and high-temperature annealing in a MBE. (b) Left panel: transmission electron micrograph (TEM) of a dewetted island. Right panel: high-resolution TEM highlighting the interface between BOX, some pristine UT SOI, and $Si_{0.7}Ge_{0.3}$. (c) Scanning electron micrographs (SEM) of 150 nm $Si_{0.7}Ge_{0.3}$ on UT SOI after 4 h annealing at a nominal temperature of 800 °C (measured with a pyrometer at the center of the sample). Left to right: morphologies observed from the edge to the center of the sample, respectively taken at 150, 500, 920, 1800, and 7500 μm from the sample edge (the latter being unchanged up to the center and starting at ~3 mm from the edge). They account for a temperature gradient of about 50 °C and allow to monitor a smooth change in a single experiment.

undergo spinodal solid-state dewetting, as in Refs. [20,21,25], and (2) the process leads to morphologies featuring different topology (connected or disconnected structures), size (from 0.1 up to 10 μm), and a strong hyperuniform character. These properties are shown for $Si_{1-x}Ge_x$ layers (with $x = 0.3$ to 1) deposited on ultrathin silicon on insulator (UT SOI). Three-dimensional phase-field simulations map the experimental observations. Exploiting Minkowski functionals, the arrangement of the resulting structures is shown to deviate from random patterns. Their effective hyperuniformity is assessed through metrics derived by a spectral-density analysis [23,27].

The experimental system is illustrated in Fig. 1(a): $Si_{1-x}Ge_x$-based thin films ($x = 0.3$–1, thickness 5–2000 nm), are deposited in a molecular beam epitaxy reactor (MBE) on 14 nm thick monocrystalline UT SOI (on 25 nm thick buried oxide, BOX) previously diced in 2 cm × 2 cm samples. Here, they undergo high-temperature annealing (400–800 °C for 0.5–6 h) under ultrahigh vacuum (~10^{-10} Torr).

A representative set of structures obtained by dewetting is reported in Figs. 1(b) and 1(c): exploiting a temperature gradient from the sample edge toward its center (roughly of about 50 °C) we observe a continuous morphological change of the sample surface from holes to connected (noodlelike) structures, and finally, isolated islands. A similar sequence of structures can be obtained by focusing on the same region in the sample after annealing at different temperature (see other experiments in the following). When using thick $Si_{0.7}Ge_{0.3}$ layers (e.g., > 200 nm), after dewetting, we observe structures with threading dislocations propagating along the (111) plane [Fig. 1(b)], as expected in crystalline bilayer systems with lattice mismatch.

Surface corrugations [28] and island formation [29,30] in strained $Si_{1-x}Ge_x$ films on Si (with partial or absent plastic relaxation) are commonly described by the Asaro-Tiller-Grinfeld (ATG) instability [31–33], i.e., as the growth of 3D structures relaxing in-plane strains with a periodicity determined by the balance between elastic and surface energy. On bulk Si, trenches between islands form and deepen within the substrate while mass can flow across them. No dewetting occurs while coarsening takes place on a bulk substrate. The key difference in the process illustrated in Fig. 1 is the use of UT SOI: the ATG instability provides the driving force for digging into the UT SOI, suddenly uncovers the BOX underneath and there initiates solid-state dewetting.

This dewetting instability is simultaneous across the sample (in contrast with conventional solid-state dewetting [25,26,34–36]) and we term the process illustrated in Fig. 1 *spinodal solid state dewetting* due to the morphology of the resulting disordered structures: in spite of the different forces at play and material-transport mechanisms, they resemble those obtained in thin films of polymers and liquid metals [17,18,20,37–39].

Patterns qualitatively similar to the experimental ones are reproduced by a minimal phase-field (PF) model, which

accounts for the energetics of surfaces, favoring surface smoothing by surface diffusion and the competing relaxation of biaxial (misfit) strain, favoring surface corrugations as in the context of the ATG instability [31–33]. The considered PF model describes these contributions and tracks the surface Σ of the film as the 0.5 level set of a continuous variable φ set to 1 in $Si_{1-x}Ge_x$ and UT SOI, and 0 in vacuum, while changing smoothly in between over a length ϵ [40,41]. The model reads

$$\partial_t \varphi = D\nabla \cdot \left(\frac{1}{\epsilon} M(\varphi) \nabla \omega\right),$$
$$g(\varphi)\omega = \gamma\left(-\epsilon \nabla^2 \varphi + \frac{1}{\epsilon} F'(\varphi)\right) + \frac{\partial \rho_e(\varphi, \boldsymbol{\varepsilon})}{\partial \varphi}, \quad (1)$$

with ω the chemical potential, $M(\varphi) = 36\varphi^2(1-\varphi)^2$ a mobility function, $F(\varphi) = 18\varphi^2(1-\varphi)^2$ a double-well potential, $g(\varphi) = 30\varphi^2(1-\varphi)^2$ a stabilization function, D a diffusion coefficient (incorporated in the timescale $t' = t/D$) [40,41], and γ the isotropic surface-energy density. $\partial \rho_e(\varphi, \boldsymbol{\varepsilon})/\partial\varphi$ encodes the elastic-energy contribution (toward roughening) to the chemical potential, with $\rho_e(\varphi, \boldsymbol{\varepsilon}) = \boldsymbol{\varepsilon} : \boldsymbol{\sigma}(\varphi, \boldsymbol{\varepsilon})$ the elastic-energy density, $\boldsymbol{\sigma}(\varphi, \boldsymbol{\varepsilon}) = \mathbf{C}(\varphi) : \boldsymbol{\varepsilon}$ the stress field, $\boldsymbol{\varepsilon} = (1/2)[\nabla \mathbf{u} + (\nabla \mathbf{u})^T] + h(\varphi)\varepsilon_0 \mathbf{I}$ the strain field, $\mathbf{u}$ the displacement with respect to the relaxed state, $\mathbf{C}(\varphi)$ the elastic constant tensor, and $h(\varphi)$ an auxiliary function vanishing in the vacuum phase. ε_0 is the effective misfit strain between $Si_{1-x}Ge_x$ and UT SOI (residual in the presence of plastic relaxation). $\boldsymbol{\varepsilon}$ is determined by solving the mechanical equilibrium equation $\nabla \cdot \boldsymbol{\sigma}(\varphi, \mathbf{u}) = 0$ [40,42]. Because of its very small relative thickness, the Si layer is not explicitly considered, but its presence is encoded in ε_0 by strain accumulation. For the asymptotic analysis $\epsilon \to 0$ we refer to [40,43,44]. The amorphous buried oxide is modeled through a no-flux boundary condition for φ [45,46] allowing for dewetting and enforcing a 90° contact angle, without loss of generality [46,47]. Other effects, such as plastic relaxation and intermixing, can be treated as changes in the eigenstrain in a mean-field approximation [48]. We express the system size (such as thickness h, and lateral extension L) in terms of the characteristic ATG length $\ell = \gamma/\rho_{\text{flat}}$, with ρ_{flat} the elastic-energy density of a flat film under biaxial strain [31–33]. Numerical simulations are performed using the parallel finite element toolbox AMDiS [49,50] with adaptive time steps and mesh refinement (see also [42,47,51] and Supplemental Material, SM [52]). Model extensions to consider the substrate or a second solid phase [48,53,54], alloys [55], surface-energy anisotropy leading to surface faceting [51,56,57], and different contact angles [47] can be considered.

In agreement with the ATG instability, well describing the early evolution of a perturbed film, the corrugation has a characteristic wavelength ℓ and amplifies over time (Fig. 2) [58]. When the trenches reach the BOX, dewetting sets in everywhere and almost simultaneously in the film. Despite the simplified model, the main features of the dewetting dynamics are qualitatively reproduced for different film thicknesses, annealing time, and temperature (accounted for by the diffusion coefficient D depending on temperature by an Arrhenius law [59]).

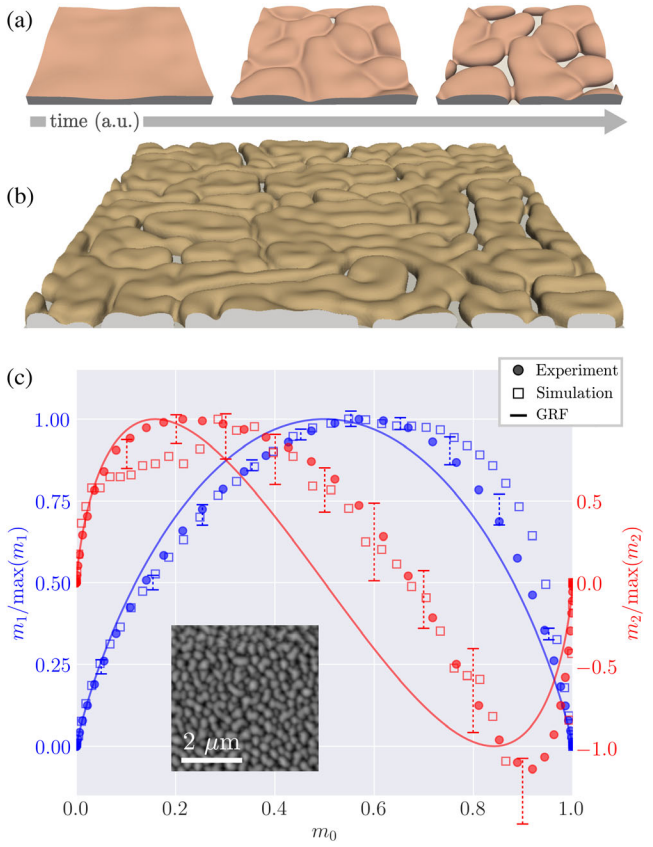

FIG. 2. Simulations and pattern analysis. (a) Breakup of a perturbed film ($h = 0.25\ell$, $L = 4\ell$, details on ℓ in the text). (b) Simulated sample for pattern analysis ($h = 0.5\ell$, $L = 20\ell$). (c) Analysis by Minkowski functionals [$m_1(\bar{\rho})$ and $m_2(\bar{\rho})$ vs $m_0(\bar{\rho})$] for the pattern of (b) (open squares) and experimental data (filled dots), corresponding to 25 nm Ge deposited on UT SOI and annealed at 470 °C for 45 min. The inset shows a $1/10 \times 1/10$ portion of the full image (reported in the Supplemental Material, SM [52]). The error bars show the variability of $m_1(m_0)$ and $m_2(m_0)$ with different spinodal-like patterns (not shown). Solid lines correspond to the expected values for a Gaussian random field (GRF) [39].

The morphology and nature of disorder of the dewetted structures in experiments and simulations are analyzed by Minkowski functionals, that quantify the topological properties and, in turn, spatial features of 2D patterns [17,60,61]. We consider averaged Minkowski functionals [39] (see also SM [52]) $m_i(\bar{\rho}) = (1/|\Omega|)M_i(\mathcal{B}_{\bar{\rho}})$ of thresholded 8-bit gray-scale images representing the thickness of samples by a space-dependent field $\rho(\mathbf{p}_{ij}) \in [0, 255]$, with $\mathbf{p}_{ij}$ the coordinate of image pixels, over a region with extension $|\Omega|$. $\bar{\rho}$ is a given threshold defining a binary

image as $\mathcal{B}_{\bar{\rho}} = \Theta[\rho(\mathbf{p}_{ij}) - \bar{\rho}]$ and Θ the Heavyside function. $m_0(\bar{\rho})$ corresponds to the fraction of $|\Omega|$ occupied by the nonzero region in $\mathcal{B}_{\bar{\rho}}$, as $M_0(\mathcal{B}_{\bar{\rho}})$ gives the area occupied by $\mathcal{B}_{\bar{\rho}} = 1$. $m_1(\rho)$ represents an average of the boundary length U between the regions $\mathcal{B}_{\bar{\rho}} = 1$ and $\mathcal{B}_{\bar{\rho}} = 0$, as $U = 2\pi M_1(\mathcal{B}_{\bar{\rho}})$. Similarly, $m_2(\rho)$ corresponds to the averaged Euler characteristic χ, as $\chi = \pi M_2(\mathcal{B}_{\bar{\rho}})$. The plot of $m_{1,2}(m_0)$ with the encoded averaging, provides results independent of image saturation and contrast [39].

$m_{1,2}(m_0)$ for representative experimental and simulated patterns almost overlap for most of the m_0 range (Fig. 2). Different experimental connected and disconnected structures follow a similar behavior [see the range of variation highlighted by dashed error bars in Fig. 2(c)]. $m_{1,2}(m_0)$ assesses the deviation from a Gaussian random field (solid lines) [39]. This deviation points to nonlinearity of the underlying dynamics and correlations in the resulting patterns (for a similar analysis, see [38]).

Based on the theoretical prediction in Refs. [23] and [27], we further assess the correlation properties of the dewetted structures by looking at the spectral density $\psi^*(|\mathbf{k}|)$ with $\mathbf{k} = (k_x, k_y)$ [Figs. 3(a) and 3(b)] of their correlation function $\psi(x, y)$ obtained from a given height profile $Z(x, y)$ [inset of Fig. 2(c)] and, in particular, at its decay for small wave numbers (long wavelength) [23,27,62]. Patterns can be considered to be hyperuniform if $\psi^*(|\mathbf{k}|/\bar{k}) = (|\mathbf{k}|/\bar{k})^\beta$ and $\beta \geq 4$ with $|\mathbf{k}|/\bar{k} \to 0$ ($\bar{k}$ is the position of the maximum in the reciprocal space). $\beta = 4$ corresponds to a Gaussian random field whereas larger values occur in the presence of correlations leading to stronger suppression of long wavelengths oscillations [2,3]. For the morphology shown in the inset of Fig. 2(c) we obtain $5 < \beta < 6$ for $0.1 < |\mathbf{k}|/\bar{k} < 1$ [Fig. 3(b)]. In most of the analyzed patterns $\beta \sim 6$ when considering sufficiently large images Whereas hyperuniform structures present a ratio $H = \psi^*(0^+)/\psi^*(\bar{k})$ strictly equal to zero, a $H \leq 10^{-4}$ [as in Fig. 3(c)] is accepted to be a fingerprint of hyperuniformity, at least for real systems [2,3] and in the presence of other arguments supporting long-range interactions and correlations [63]. Indeed, inherent spurious effects arising from image thresholding [23] affect the steep decrease of $\psi^*(|\mathbf{k}|)$ for smaller $\mathbf{k}$ [Figs. 2(d) and 2(e)]. We thus consider the emergent patterns by spinodal solid-state dewetting as hyperuniform.

The degree of hyperuniformity can be tuned by considering different temperature and thus, different stages during the dewetting process [see Fig. 3(d), obtained by considering samples with $x = 1$, thickness of 50 nm and changing the annealing condition]. Larger and disconnected structures behave more like a GRF ($\beta \sim 4$), whereas for more connected structures a marked hyperuniformity emerges ($\beta \sim 5$–6). We can also replicate morphologies featuring a similar hyperuniform character [e.g., $\beta \sim 6$, Fig. 3(e)] but different $\bar{k}$, i.e., peak position of $\psi_Z^*(|\mathbf{k}|)$ obtained by dewetting Ge layers having different initial thickness

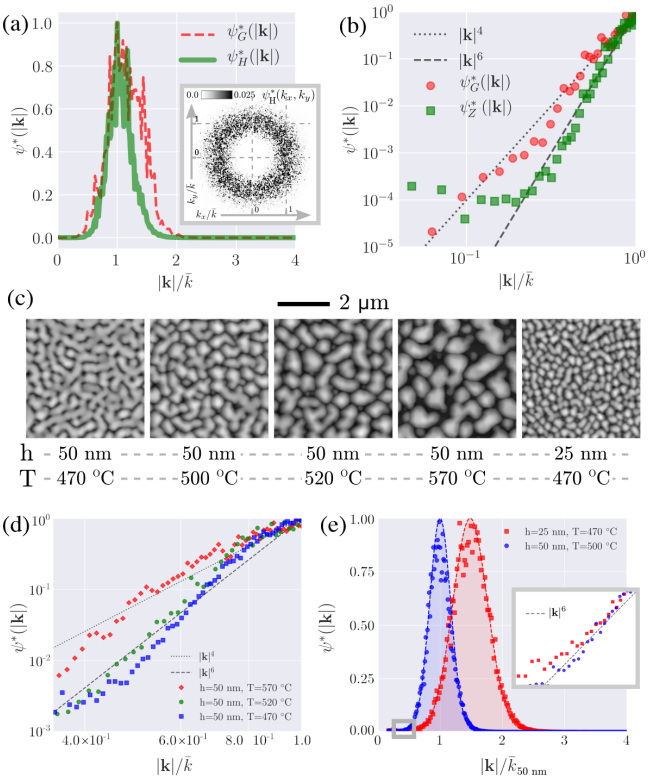

FIG. 3. Hyperuniformity and tuning of the disorder: (a) Radial spectral density $\psi^*(|\mathbf{k}|)$ for the pattern of Fig. 2(c) [$\psi_H^*(|\mathbf{k}|)$] and a numerically generated GRF [$\psi_G^*(|\mathbf{k}|)$], with the inset showing $\psi_H^*(k_x, k_y)$. (b) Logarithmic plot of data in panel (a) highlighting the decay of $\psi^*(|\mathbf{k}|)$ for $|\mathbf{k}| \to 0$. Dashed and dotted lines are the trend of $|\mathbf{k}|^4$ and $|\mathbf{k}|^6$, respectively. (c) AFM images of Ge ($h = 50$ nm and 25 nm) deposited on UT SOI and annealed at different temperature. (d) Logarithmic plot of experimental $\psi_Z^*(|\mathbf{k}|)$ for similar samples annealed at different temperature [see panel (c), corresponding large view 40 μm $\times$ 40 μm AFM images have been used]. (e) Comparison of $\psi_Z^*(|\mathbf{k}|)$ of the patterns in the two last panels of (c).

[Fig. 3(c), respectively 50 nm, $T = 500\,°\text{C}$ and 25 nm, $T = 470\,°\text{C}$]. This demonstrates a size tuning of structures exhibiting similar correlations.

In conclusion, we identified an elasticity-driven instability in strained, thin films undergoing solid-state dewetting, enabling the formation of spinodal, monocrystalline patterns that exhibit effective hyperuniformity. The process is scalable, as it does not depend on the sample size and, more importantly, adjustable: setting layer thickness and annealing cycle provides structures with different topology (connected to disconnected), composition (from $Si_{0.7}Ge_{0.3}$ to pure Ge), and size (from hundreds of nanometers to tens of micrometers). Examples are provided at a glance in the SM [52]. The class of hyperuniform materials, including so-far various natural and artificial systems, such as, polymer-grafted nanoparticles [64], polymer melt [65], colloid deposition [4], maximally random jammed packing [66], clusters of nanoparticles [67], and foams [68] has

then been extended to technology-relevant materials. Furthermore, a remarkable advantage of spinodal solid-state dewetting for hyperuniform materials over conventional processes at critical points [23,24] is the possibility to freeze the system in a desired condition, thus setting at will its properties.

The choice of a UT SOI substrate and $Si_{1-x}Ge_x$ alloys, which are common and cost-effective materials, opens the path to fruitful industrialization as a realistic platform for electricity, light, or matter management. Moreover, the fabrication of hyperuniform devices has been attempted with more or less cumbersome top-down approaches over limited extensions [7,12,13,69] and, in this respect, the reported dewetting process is more convenient, as it can be implemented in a single fabrication step and results in atomically smooth monocrystals having, for instance, superior electronic figures of merits with respect to rough, etched materials [36].

We acknowledge fruitful discussions with Marian Florescu (University of Surrey), Riccardo Sapienza (Imperial College London), Massimo Gurioli and Dominique Chatain (CINAM, Marseille). This research was funded by the EU H2020 FET-OPEN project NARCISO (No. 828890). J. W. and J.-B. C. acknowledge the European Research Council (ERC, Grant Agreement No. 723241). A. B. and M. A. acknowledge PRCI network ULYSSES (ANR-15-CE24-0027-01) funded by the French ANR agency. We gratefully acknowledge the computing time granted by Julich Supercomputing Centre (JSC) within Project No. HDR06, and by ZIH at TU Dresden. We acknowledge the Nanotecmat platform of the IM2NP institute of Marseilles and the microscopy center of Aix-Marseille University CP2M.

*marco.salvalaglio@tu-dresden.de
†monica.bollani@ifn.cnr.it
‡marco.abbarchi@im2np.fr

[1] S. Torquato and F. H. Stillinger, Local density fluctuations, hyperuniformity, and order metrics, Phys. Rev. E **68**, 041113 (2003).
[2] S. Torquato, Hyperuniform states of matter, Phys. Rep. **745**, 1 (2018).
[3] M. A. Klatt, J. Lovrić, D. Chen, S. C. Kapfer, F. M. Schaller, P. W. Schönhöfer, B. S. Gardiner, A.-S. Smith, G. E. Schröder-Turk, and S. Torquato, Universal hidden order in amorphous cellular geometries, Nat. Commun. **10**, 811 (2019).
[4] P. M. Piechulla, L. Muehlenbein, R. B. Wehrspohn, S. Nanz, A. Abass, C. Rockstuhl, and A. Sprafke, Fabrication of nearly-hyperuniform substrates by tailored disorder for photonic applications, Adv. Opt. Mater. **6**, 1701272 (2018).
[5] N. P. Mitchell, L. M. Nash, D. Hexner, A. M. Turner, and W. T. Irvine, Amorphous topological insulators constructed from random point sets, Nat. Phys. **14**, 380 (2018).
[6] Y. A. Gerasimenko, I. Vaskivskyi, M. Litskevich, J. Ravnik, J. Vodeb, M. Diego, V. Kabanov, and D. Mihailovic, Quantum jamming transition to a correlated electron glass in 1T-TaS_2, Nat. Mater. **18**, 1078 (2019).
[7] L. S. Froufe-Pérez, M. Engel, J. J. Sáenz, and F. Scheffold, Band gap formation and Anderson localization in disordered photonic materials with structural correlations, Proc. Natl. Acad. Sci. U.S.A. **114**, 9570 (2017).
[8] W. Zhou, Z. Cheng, B. Zhu, X. Sun, and H. K. Tsang, Hyperuniform disordered network polarizers, IEEE J. Sel. Top. Quantum Electron. **22**, 288 (2016).
[9] R. DeglInnocenti, Y. Shah, L. Masini, A. Ronzani, A. Pitanti, Y. Ren, D. Jessop, A. Tredicucci, H. E. Beere, and D. A. Ritchie, Hyperuniform disordered terahertz quantum cascade laser, Sci. Rep. **6**, 19325 (2016).
[10] M. Florescu, S. Torquato, and P. J. Steinhardt, Designer disordered materials with large, complete photonic band gaps, Proc. Natl. Acad. Sci. U.S.A. **106**, 20658 (2009).
[11] W. Man, M. Florescu, E. P. Williamson, Y. He, S. R. Hashemizad, B. Y. Leung, D. R. Liner, S. Torquato, P. M. Chaikin, and P. J. Steinhardt, Isotropic band gaps and freeform waveguides observed in hyperuniform disordered photonic solids, Proc. Natl. Acad. Sci. U.S.A. **110**, 15886 (2013).
[12] N. Muller, J. Haberko, C. Marichy, and F. Scheffold, Silicon hyperuniform disordered photonic materials with a pronounced gap in the shortwave infrared, Adv. Opt. Mater. **2**, 115 (2014).
[13] L. S. Froufe-Pérez, M. Engel, P. F. Damasceno, N. Muller, J. Haberko, S. C. Glotzer, and F. Scheffold, Role of Short-Range Order and Hyperuniformity in the Formation of Band Gaps in Disordered Photonic Materials, Phys. Rev. Lett. **117**, 053902 (2016).
[14] M. C. Cross and P. C. Hohenberg, Pattern formation outside of equilibrium, Rev. Mod. Phys. **65**, 851 (1993).
[15] P. Ball and N. R. Borley, *The Self-Made Tapestry: Pattern Formation in Nature* (Oxford University Press, Oxford, 1999), Vol. 198.
[16] A. M. Turing, The chemical basis of morphogenesis, Bull. Math. Biol. **52**, 153 (1990).
[17] J. Becker, G. Grün, R. Seemann, H. Mantz, K. Jacobs, K. R. Mecke, and R. Blossey, Complex dewetting scenarios captured by thin-film models, Nat. Mater. **2**, 59 (2003).
[18] N. Stoop, R. Lagrange, D. Terwagne, P. M. Reis, and J. Dunkel, Curvature-induced symmetry breaking determines elastic surface patterns, Nat. Mater. **14**, 337 (2015).
[19] J. W. Cahn, On spinodal decomposition, Acta Metall. **9**, 795 (1961).
[20] S. Herminghaus, K. Jacobs, K. Mecke, J. Bischof, A. Fery, M. Ibn-Elhaj, and S. Schlagowski, Spinodal dewetting in liquid crystal and liquid metal films, Science **282**, 916 (1998).
[21] R. Xie, A. Karim, J. F. Douglas, C. C. Han, and R. A. Weiss, Spinodal Dewetting of Thin Polymer Films, Phys. Rev. Lett. **81**, 1251 (1998).
[22] A. M. Higgins and R. A. Jones, Anisotropic spinodal dewetting as a route to self-assembly of patterned surfaces, Nature (London) **404**, 476 (2000).
[23] Z. Ma and S. Torquato, Random scalar fields and hyperuniformity, J. Appl. Phys. **121**, 244904 (2017).
[24] Z. Ma, E. Lomba, and S. Torquato, Optimized Large Hyperuniform Binary Colloidal Suspensions in Two Dimensions, Phys. Rev. Lett. **125**, 068002 (2020).

[25] C. V. Thompson, Solid-state dewetting of thin films, Annu. Rev. Mater. Res. **42**, 399 (2012).
[26] M. Naffouti, T. David, A. Benkouider, L. Favre, A. Ronda, I. Berbezier, S. Bidault, N. Bonod, and M. Abbarchi, Fabrication of poly-crystalline Si-based Mie resonators via amorphous Si on SiO_2 dewetting, Nanoscale **8**, 7768 (2016).
[27] S. Torquato, Hyperuniformity and its generalizations, Phys. Rev. E **94**, 022122 (2016).
[28] J. Frigerio, M. Lodari, D. Chrastina, V. Mondiali, G. Isella, and M. Bollani, Metastability and relaxation in tensile SiGe on Ge (001) virtual substrates, J. Appl. Phys. **116**, 113507 (2014).
[29] J.-N. Aqua, I. Berbezier, L. Favre, T. Frisch, and A. Ronda, Growth and self-organization of SiGe nanostructures, Phys. Rep. **522**, 59 (2013).
[30] A. Shklyaev and A. Latyshev, Surface morphology transformation under high-temperature annealing of Ge layers deposited on Si (100), Nanoscale Res. Lett. **11**, 366 (2016).
[31] R. J. Asaro and W. A. Tiller, Interface morphology development during stress corrosion cracking: Part I. Via surface diffusion, Metall. Mater. Trans. B **3**, 1789 (1972).
[32] M. A. Grinfeld, The stress driven instability in elastic crystals: Mathematical models and physical manifestations, J. Nonlinear Sci. **3**, 35 (1993).
[33] D. J. Srolovitz, On the stability of surfaces of stressed solids, Acta Metall. **37**, 621 (1989).
[34] J. Ye and C. V. Thompson, Templated solid-state dewetting to controllably produce complex patterns, Adv. Mater. **23**, 1567 (2011).
[35] J. Ye, D. Zuev, and S. Makarov, Dewetting mechanisms and their exploitation for the large-scale fabrication of advanced nanophotonic systems, Int. Mater. Rev. **64**, 439 (2019).
[36] M. Bollani, M. Salvalaglio, A. Benali, M. Bouabdellaoui, M. Naffouti, M. Lodari, S. Di Corato, A. Fedorov, A. Voigt, I. Fraj, L. Favre, J. B. Claude, D. Grosso, G. Nicotra, A. Mio, A. Ronda, I. Berbezier, and M. Abbarchi, Templated dewetting of single-crystal, ultra-long nanowires and on-chip silicon circuits, Nat. Commun. **10**, 5632 (2019).
[37] M. Heurlin, M. H. Magnusson, D. Lindgren, M. Ek, L. R. Wallenberg, K. Deppert, and L. Samuelson, Continuous gas-phase synthesis of nanowires with tunable properties, Nature (London) **492**, 90 (2012).
[38] H. Galinski, A. Ambrosio, P. Maddalena, I. Schenker, R. Spolenak, and F. Capasso, Instability-induced pattern formation of photoactivated functional polymers, Proc. Natl. Acad. Sci. U.S.A. **111**, 17017 (2014).
[39] H. Mantz, K. Jacobs, and K. Mecke, Utilizing Minkowski functionals for image analysis: A marching square algorithm, J. Stat. Mech. (2008) P12015.
[40] A. Rätz, A. Ribalta, and A. Voigt, Surface evolution of elastically stressed films under deposition by a diffuse interface model, J. Comput. Phys. **214**, 187 (2006).
[41] B. Li, J. Lowengrub, A. Ratz, and A. Voigt, Review article: Geometric evolution laws for thin crystalline films: Modeling and numerics, Commun. Comput. Phys. **6**, 433 (2009), http://www.global-sci.com/intro/article_detail.html?journal=cicp&article_id=7688.
[42] R. Bergamaschini, M. Salvalaglio, R. Backofen, A. Voigt, and F. Montalenti, Continuum modelling of semiconductor heteroepitaxy: An applied perspective, Adv. Phys. X **1**, 331 (2016).
[43] A. Voigt, Comment on "Degenerate mobilities in phase field models are insufficient to capture surface diffusion", Appl. Phys. Lett. **107**, 081603 (2015); **108**, 036101 (2016).
[44] M. Salvalaglio, A. Voigt, and S. Wise, Doubly degenerate diffuse interface models of surface diffusion, arXiv:1909.04458.
[45] W. Jiang, W. Bao, C. V. Thompson, and D. J. Srolovitz, Phase field approach for simulating solid-state dewetting problems, Acta Mater. **60**, 5578 (2012).
[46] M. Naffouti, R. Backofen, M. Salvalaglio, T. Bottein, M. Lodari, A. Voigt, T. David, A. Benkouider, I. Fraj, L. Favre, A. Ronda, I. Berbezier, D. Grosso, M. Abbarchi, and M. Bollani, Complex dewetting scenarios of ultrathin silicon films for large-scale nanoarchitectures, Sci. Adv. **3**, eaao1472 (2017).
[47] R. Backofen, S. M. Wise, M. Salvalaglio, and A. Voigt, Convexity splitting in a phase field model for surface diffusion, Int. J. Numer. Anal. Model. **16**, 192 (2019), https://www.global-sci.org/intro/article_detail/ijnam/12799.html.
[48] M. Salvalaglio, P. Zaumseil, Y. Yamamoto, O. Skibitzki, R. Bergamaschini, T. Schroeder, A. Voigt, and G. Capellini, Morphological evolution of Ge/Si nano-strips driven by Rayleigh-like instability, Appl. Phys. Lett. **112**, 022101 (2018).
[49] S. Vey and A. Voigt, AMDiS: Adaptive multidimensional simulations, Comput. Visual. Sci. **10**, 57 (2007).
[50] T. Witkowski, S. Ling, S. Praetorius, and A. Voigt, Software concepts and numerical algorithms for a scalable adaptive parallel finite element method, Adv. Comput. Math. **41**, 1145 (2015).
[51] M. Salvalaglio, R. Backofen, R. Bergamaschini, F. Montalenti, and A. Voigt, Faceting of equilibrium and metastable nanostructures: A phase-field model of surface diffusion tackling realistic shapes, Cryst. Growth Des. **15**, 2787 (2015).
[52] See Supplemental Material at http://link.aps.org/supplemental/10.1103/PhysRevLett.125.126101 for further information on high resolution electron micrograph imaging, phase field simulations and data analysis.
[53] S. M. Wise, J. S. Lowengrub, J. S. Kim, K. Thornton, P. W. Voorhees, and W. C. Johnson, Quantum dot formation on a strain-patterned epitaxial thin film, Appl. Phys. Lett. **87**, 133102 (2005).
[54] M. Albani, R. Bergamaschini, and F. Montalenti, Dynamics of pit filling in heteroepitaxy via phase-field simulations, Phys. Rev. B **94**, 075303 (2016).
[55] R. Backofen, R. Bergamaschini, and A. Voigt, The interplay of morphological and compositional evolution in crystal growth: A phase-field model, Philos. Mag. **94**, 2162 (2014).
[56] S. Torabi, J. Lowengrub, A. Voigt, and S. Wise, A new phase-field model for strongly anisotropic systems, Proc. R. Soc. A **465**, 1337 (2009).
[57] M. Salvalaglio, R. Backofen, A. Voigt, and F. Montalenti, Morphological evolution of pit-patterned Si(001) substrates

driven by surface-energy reduction, Nanoscale Res. Lett. **12**, 554 (2017).

[58] Results in terms of wavelength and emerging patterns are independent on the initial perturbation, provided that it contains wavelengths smaller than ℓ. For wavelengths larger than ℓ, stripes are obtained (see Supplemental Material [52]).

[59] W. W. Mullins, Theory of thermal grooving, J. Appl. Phys. **28**, 333 (1957).

[60] H. Minkowski, Volumen und Oberfläche, in *ausgewählte Arbeiten zur Zahlentheorie und zur Geometrie* (Springer, Vienna, 1989), pp. 146–192.

[61] R. Schneider, *Convex Bodies: The Brunn-Minkowski Theory* (Cambridge University Press, Cambridge, 2014).

[62] T. Gruhn, E. Pogorelov, F. Seiferling, and H. Emmerich, Analyzing spinodal decomposition of an anisotropic fluid mixture, J. Phys. Condens. Matter **29**, 055103 (2016).

[63] Y. Jiao, T. Lau, H. Hatzikirou, M. Meyer-Hermann, J. C. Corbo, and S. Torquato, Avian photoreceptor patterns represent a disordered hyperuniform solution to a multiscale packing problem, Phys. Rev. E **89**, 022721 (2014).

[64] A. Chremos and J. F. Douglas, Particle localization and hyperuniformity of polymer-grafted nanoparticle materials, Ann. Phys. (Amsterdam) **529**, 1600342 (2017).

[65] W.-S. Xu, J. F. Douglas, and K. F. Freed, Influence of cohesive energy on the thermodynamic properties of a model glass-forming polymer melt, Macromolecules **49**, 8341 (2016).

[66] S. Atkinson, G. Zhang, A. B. Hopkins, and S. Torquato, Critical slowing down and hyperuniformity on approach to jamming, Phys. Rev. E **94**, 012902 (2016).

[67] C. De Rosa, F. Auriemma, C. Diletto, R. Di Girolamo, A. Malafronte, P. Morvillo, G. Zito, G. Rusciano, G. Pesce, and A. Sasso, Toward hyperuniform disordered plasmonic nanostructures for reproducible surface-enhanced Raman spectroscopy, Phys. Chem. Chem. Phys. **17**, 8061 (2015).

[68] J. Ricouvier, P. Tabeling, and P. Yazhgur, Foam as a self-assembling amorphous photonic band gap material, Proc. Natl. Acad. Sci. U.S.A. **116**, 9202 (2019).

[69] M. Castro-Lopez, M. Gaio, S. Sellers, G. Gkantzounis, M. Florescu, and R. Sapienza, Reciprocal space engineering with hyperuniform gold disordered surfaces, APL Photonics **2**, 061302 (2017).